

Whole-Body Human Ultrasound Tomography

David C. Garrett[†], Jinhua Xu[†], Geng Ku, and Lihong V. Wang*

Caltech Optical Imaging Laboratory, Andrew and Peggy Cherng Department of Medical Engineering, Department of Electrical Engineering, California Institute of Technology, Pasadena, CA 91125 USA

[†] These authors contributed equally.

* Corresponding author: lvw@caltech.edu

Abstract

We developed a system for whole-body human ultrasound tomography in reflection and transmission modes. A custom 512-element ultrasound receiver array with a rotating single-element ultrasound transmitter are used to generate 2D isotropically resolved images across the entire human cross-section. We demonstrate this technique in regions such as the abdomen and legs in healthy volunteers. Compared to handheld-probe-based ultrasonography, this approach provides a substantially larger field of view, depends less on operator training, and obtains quantitative tissue parameter profiles in addition to reflectivity images. Whole-body ultrasound tomography could be valuable in applications such as organ disease screening, image-guided needle biopsy, and treatment monitoring.

Introduction

Since its inception in the mid-20th century, ultrasound imaging has revolutionized healthcare by providing rapid and affordable insight into tissue structure and function. Early systems employed single transducers scanned linearly or circularly with subjects immersed in a water bath [1], [2], later followed by membrane approaches to image regions in the abdomen [3]. Initial results were promising for disease diagnosis [4], but bulky electronics and slow acquisition times necessitated mechanical scanning over several minutes. Later developments in transducers and electronics led to linear probes [5], where multiple channels could be used in parallel. The handheld probe remains the most used form of ultrasonography and has found many clinical applications. However, probes require trained operation [6], provide only reflection-mode images over a narrow field of view (FOV), and have limited ability to visualize features behind bone or air pockets.

More recently, alternate approaches using smaller immersion tanks with planar [7], linear [8], ring [9], or hemispherical [10] transducer arrays have been investigated for ultrasound tomography (UST) imaging of the breast [11] or limbs of the body. These systems record both reflected and transmitted signals, allowing for reflectivity, speed of sound, and attenuation profiles to be recovered. In extending to human-scale imaging, acoustically opaque regions like bone or air pockets have been conventionally viewed as insurmountable obstacles. A recent study achieved whole-body imaging in piglets despite the presence of bone and air [12]. Another recent system enables volumetric reflection-mode imaging of human extremities like the arm, visualizing vasculature and bones [13]. However, these system geometries and parameters (e.g., acoustic frequency, transmitter power, and detection sensitivity) are not yet suitable for whole-body human imaging.

In this work, we return to geometries like those used by the early ultrasonography practitioners but with the advantage of modern electronics and transducer technology. We employ a custom circular array with 512 receiver elements combined with a single-element transmitter which rotates around the subject. This configuration allows for whole-body UST imaging of humans immersed in water, resulting 2D isotropic images of reflectivity, speed of sound, and attenuation profiles. Using full 360° viewing angles, we overcome acoustic penetration through tissues such as bone or air pockets. We demonstrate this technique by imaging regions in the abdomen and legs in healthy volunteers. Several organs and key features can be clearly observed in reflection-mode images, and we also demonstrate recovery of tissue speed of sound and attenuation.

Results

We developed a custom 60 cm diameter 512-element acoustic receiver array with 1 MHz center frequency. A 1.5-inch diameter 2.25 MHz transducer (Olympus V395) with a custom diverging cylindrical polymethylpentene (TPX) lens is used as a transmitter. The transmitter is mounted on a plastic gear which rotates around the subject using a stepper motor. The array is mounted on two vertical linear motor stages to adjust its height in a water immersion tank. Water acts as acoustic coupling between tissue and the transducers. An arbitrary function generator (Siglent SDG2042X) connected to a 300-Watt RF power amplifier (ENI 350L) excite the transmitter using a 400 μ s chirp signal spanning 0.3-2.0 MHz. The system hardware is shown in Figure 1.

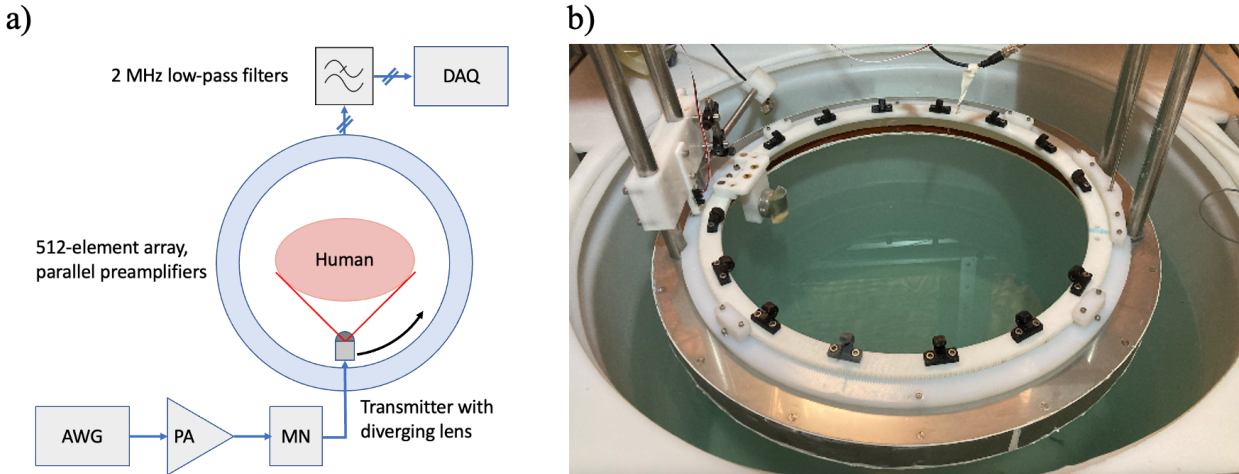


Figure 1. a) System diagram. AWG: arbitrary waveform generator; PA: power amplifier; MN: matching network; DAQ: data acquisition module. b) System photograph.

We demonstrate whole-body UST with a healthy female volunteer. The subject is seated in the water immersion tank with the head held against a cushion to reduce motion and with arms raised slightly to lift the ribs. Figure 2 shows an example reflection-mode image of the abdomen. The image is displayed in inverse grayscale (brighter regions are more anechoic) normalized to the peak pixel amplitude. Various structures are visualized, including the liver, stomach, spleen, abdominal aorta, and vertebral body. Note that despite the presence of bone and air pockets, our imaging geometry allows high fidelity imaging of regions deep in the body.

Using data collecting during the same scan, we also obtain transmission-mode profiles of the speed of sound and attenuation coefficient which are overlaid on the reflection-mode images in Figure 2. The transmission mode image reconstruction uses the filtered back projection algorithm like that used in x-ray computed tomography, where the arrival time delay and the attenuation of the subject data with respect to the homogenous data are found for each transmitter-receiver ray. Slowness and attenuation coefficient maps are solved for by multiplying the derived arrival delay and attenuation vectors to the inverse of a matrix corresponding to the crossing ray length density. Due to the large size of the data, it is not practical to store and operate on such a matrix directly. Therefore, the conjugate gradient descent algorithm is used to solve the matrix inversion. The speed of sound of map can then be obtained by inverting the slowness matrix. We observe higher tissue speed of sound in the liver which agrees with literature values of approximately 1560 m/s [14].

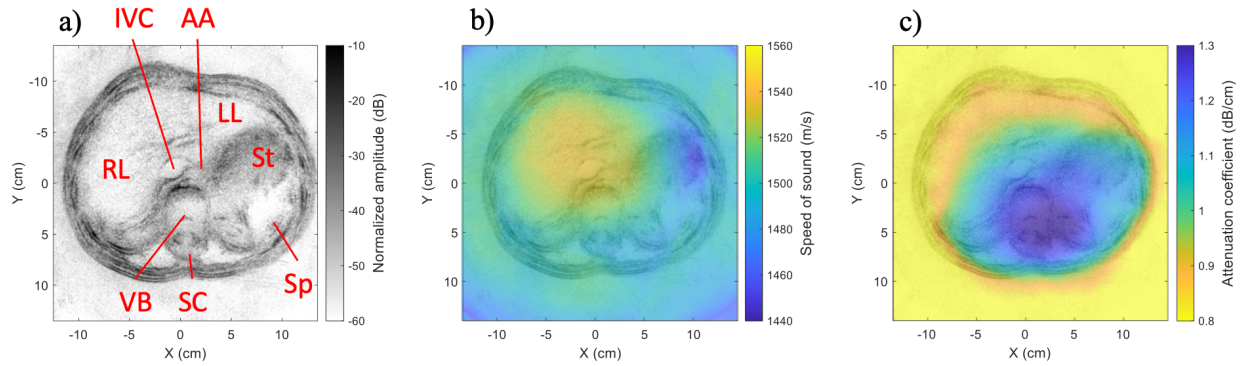


Figure 2. Example UST images. a) Reflectivity image of human abdomen. IVC: inferior vena cava. AA: abdominal aorta. RL: right lobe of liver. LL: left lobe of liver. VB: vertebral body. SC: spinal cord. St: stomach. Sp: spleen. b) and c) show the speed of sound and attenuation profiles, respectively, overlaid on the reflectivity image.

We further performed 15 scans at 1 cm vertical intervals from approximately the ribcage to the pelvis. Each scan was acquired over 10 seconds, and the subject was in the immersion tank for approximately 15 minutes. Examples of other 2D images are shown in Figure 3. Note that this volunteer previously had her left kidney removed, so only the right one is visualized.

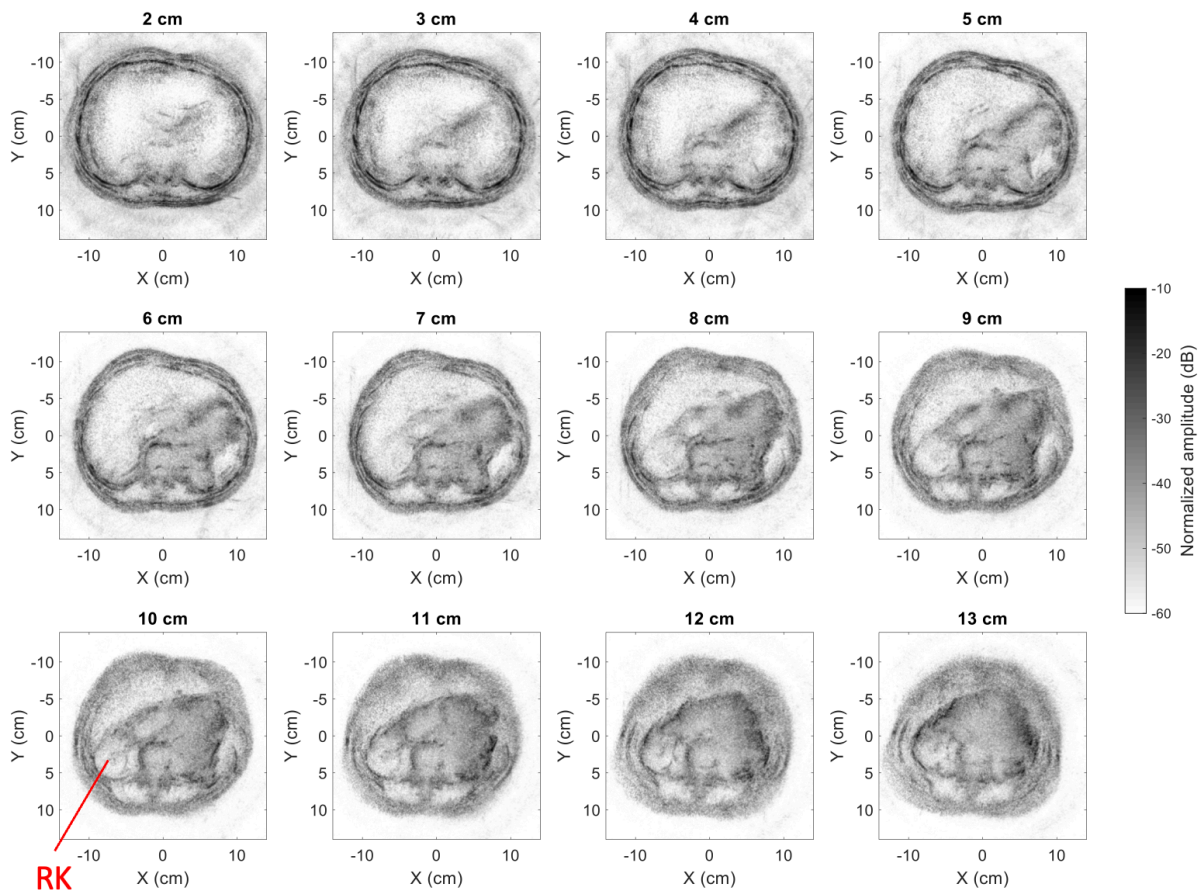


Figure 3. Example of elevational scans of a female subject from approximately the ribcage to the pelvis. RK: right kidney (left kidney was removed).

With the subject standing in the immersion tank, we also imaged the legs as shown in Figure 4. In the upper legs, the femur, surrounding muscles, and adipose boundaries are clearly observed. The tibia and fibula are visualized in the lower legs as well as adipose boundaries.

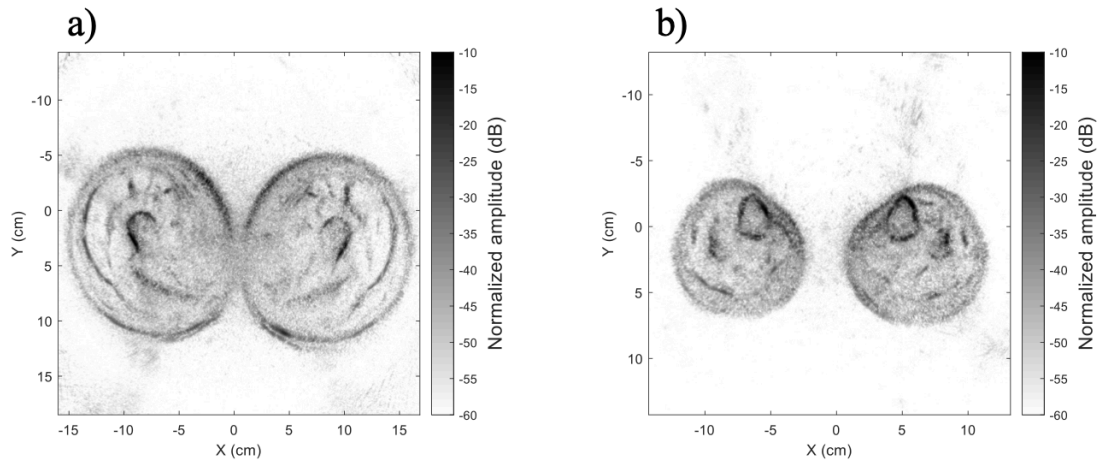


Figure 4. Reflection-mode images of a) the upper leg; and b) the lower leg of a female subject.

Discussion

We developed a system for whole-body ultrasound imaging. Compared with clinical handheld-probe-based ultrasonography, our approach images cross-sections of the whole human body and visualizes three contrasts: reflectivity, speed of sound, and attenuation. This may be of clinical use for screening organ size or structure as an early indicator of inflammation or disease [15]. The speed of sound and attenuation could also be used as diagnostic tools, for instance to assess changes due to non-alcoholic fatty liver disease. Whole-body UST could also be used in applications such as image-guided needle biopsy where x-ray computed tomography is conventionally used. With our whole-body FOV, the location of the biopsy needle could be localized with respect to tissues of interest without use of ionizing radiation.

Furthermore, clinical ultrasonography typically requires trained operation for observing regions of interest. Our approach requires only that the patient remain still, where the imaging process could then be automated. This could be an appealing feature for regular screening approaches and would help reduce the cost compared to other modalities. However, our current implementation involving patient water immersion is likely unsuitable for imaging of diseased subjects. A similar imaging geometry could therefore be implemented using water bags like those used in shockwave lithotripsy.

In the future, we plan to enhance this system with additional photoacoustic and thermoacoustic contrast. Using the same acoustic receivers, these images could be immediately co-registered with our UST images to overlay optical and microwave absorption profiles. We also aim to improve our transmission-mode reconstruction quality using techniques such as full-wave inversion [16] to better localize variations in the speed of sound and attenuation coefficient. Additional acoustic elements could also reduce image acquisition time and provide 3D imaging capability.

Materials and Methods

System hardware

All 512 receiver array elements are 3 mm × 10 mm polymer piezoelectric (PVDF-TrFE, PolyK Technologies LLC) capacitively coupled to polyimide electrodes which are directly connected to parallel preamplifiers. The preamplifiers are implemented on custom annular printed circuit boards and provide 15 dB voltage gain with 100 kΩ input impedance. The elements and preamplifiers are housed in a stainless-steel shielded enclosure. Casting epoxy is used as a backing material for each element, and an angled back panel is used to reduce reverberation. All channels are low-pass filtered ($f_c = 2$ MHz) and digitized (Photosound Legion) in parallel at 5 MSPS. The preamplifiers are powered by rechargeable lithium polymer batteries. To account for geometrical error during manufacturing, the technique described in [17] is used to calibrate each element's position.

Imaging parameters

To enhance the signal-to-noise ratio (SNR) while limited by the mechanical index, a linear chirp signal versus time (t) is used with a time varying frequency $f(t) = ct + f_0$, where $c = (f_1 - f_0)/T$ is the linear chirp rate, $f_0 = 0.3$ MHz is the lower frequency, $f_1 = 2.0$ MHz is the upper frequency, and $T = 400$ μs is the chirp duration. The transmitted frequencies are limited by the bandwidths of the transmitter and receivers. We used a maximal pulse duration given our maximal acquisition time of 800 μs, allowing for recovery of the roundtrip reflected signals over the entire field of view (FOV). The resulting transmitted chirp signal is

$$x(t) = \sin \left[2\pi \left(\frac{c}{2} t^2 + f_0 t \right) \right].$$

Compared to a pulse with similar peak pressure, this results in an expected SNR gain of $\sim \sqrt{T \cdot B}$, where $B = f_1 - f_0$ is the acoustic bandwidth. In addition to the target, we also perform a scan with only water in the imaging domain, resulting in recorded signals $x_{w,i}(t)$ for each receiver element i . This provides the response of each transducer to the chirp which is then cross-correlated with the target's chirp response $x_{c,i}(t)$. The pulse response for the target signals $\chi_{s,i}(t)$ is then recovered for each element i as:

$$\chi_{s,i}(t) = \frac{x_{w,i}(t) \star x_{c,i}(t)}{\max[x_{w,i}(t) \star x_{w,i}(t)]}$$

where \star denotes cross-correlation. We normalize by the maximum of the autocorrelation of $x_{w,i}(t)$ to account for sensitivity variation in the receiver elements. The transmitter operates with a pulse repetition rate of 180 Hz. With the gear rotation time of 10 seconds, this results in 1800 transmitted pulses over a full circular scan around the target.

Human imaging protocol

A healthy female volunteer consented to being imaged in this system. This imaging procedure was approved by the Caltech Institutional Review Board (protocol IR21-1099). Prior to human

imaging, we used a calibrated hydrophone (Onda HGL-0085) positioned immediately in front of the transmitter to evaluate the mechanical index as less than 0.2, whereas the limit from the U.S. Food and Drug Administration is 1.9 [18].

Acknowledgements

This work was supported in part by National Institutes of Health grants R35 CA220436 (Outstanding Investigator Award). L.W. has a financial interest in Microphotoacoustics, Inc., CalPACT, LLC, and Union Photoacoustic Technologies, Ltd., which, however, did not support this work.

References

- [1] J. H. Holmes and D. H. Howry, "Ultrasonic diagnosis of abdominal disease," *Am. J. Dig. Dis.*, vol. 8, no. 1, pp. 12–32, Jan. 1963, doi: 10.1007/BF02233558.
- [2] D. H. Howry and W. R. Bliss, "Ultrasonic visualization of soft tissue structures of the body," *J. Lab. Clin. Med.*, vol. 40, no. 4, pp. 579–592, 1952.
- [3] B. B. Goldberg, R. Gramiak, and A. K. Freimanis, "Early history of diagnostic ultrasound: the role of American radiologists," *AJR Am J Roentgenol*, vol. 160, no. 1, pp. 189–194, 1993.
- [4] D. H. Howry, J. H. Holmes, C. R. Cushman, and G. J. Posakony, "Ultrasonic visualization of living organs and tissues; with observations on some disease processes," *Geriatrics*, vol. 10, no. 3, pp. 123–128, Mar. 1955.
- [5] I. Donald, J. Macvicar, and T. G. Brown, "Investigation of abdominal masses by pulsed ultrasound," *Lancet Lond. Engl.*, vol. 1, no. 7032, pp. 1188–1195, Jun. 1958, doi: 10.1016/s0140-6736(58)91905-6.
- [6] J. Pinto, R. Azevedo, E. Pereira, and A. Caldeira, "Ultrasonography in Gastroenterology: The Need for Training," *GE Port. J. Gastroenterol.*, vol. 25, no. 6, pp. 308–316, Nov. 2018, doi: 10.1159/000487156.
- [7] J. Wiskin, D. T. Borup, S. A. Johnson, and M. Berggren, "Non-linear inverse scattering: High resolution quantitative breast tissue tomography," *J. Acoust. Soc. Am.*, vol. 131, no. 5, pp. 3802–3813, May 2012, doi: 10.1121/1.3699240.
- [8] L. Huang *et al.*, "Breast ultrasound tomography with two parallel transducer arrays," in *Medical Imaging 2016: Physics of Medical Imaging*, SPIE, Mar. 2016, pp. 98–109. doi: 10.1117/12.2216531.
- [9] Y. Zhang and L. Wang, "Video-Rate Ring-Array Ultrasound and Photoacoustic Tomography," *IEEE Trans. Med. Imaging*, vol. 39, no. 12, pp. 4369–4375, Dec. 2020, doi: 10.1109/TMI.2020.3017815.
- [10] N. Duric *et al.*, "Clinical breast imaging with ultrasound tomography: A description of the SoftVue system," *J. Acoust. Soc. Am.*, vol. 135, no. 4_Supplement, p. 2155, Apr. 2014, doi: 10.1121/1.4876990.
- [11] J. Wiskin *et al.*, "Full Wave 3D Inverse Scattering Transmission Ultrasound Tomography: Breast and Whole Body Imaging," in *2019 IEEE International Ultrasonics Symposium (IUS)*, Oct. 2019, pp. 951–958. doi: 10.1109/ULTSYM.2019.8925778.
- [12] J. Wiskin, B. Malik, C. Ruoff, N. Pirshafiey, M. Lenox, and J. Klock, "Whole-Body Imaging Using Low Frequency Transmission Ultrasound," *Acad. Radiol.*, Feb. 2023, doi: 10.1016/j.acra.2023.01.018.
- [13] E.-Y. Park *et al.*, "Fast volumetric ultrasound facilitates high-resolution 3D mapping of tissue compartments," *Sci. Adv.*, vol. 9, no. 22, p. eadg8176, May 2023, doi: 10.1126/sciadv.adg8176.
- [14] J. C. Bamber and C. R. Hill, "Acoustic properties of normal and cancerous human liver—I. Dependence on pathological condition," *Ultrasound Med. Biol.*, vol. 7, no. 2, pp. 121–133, Jan. 1981, doi: 10.1016/0301-5629(81)90001-6.

- [15] M. Allocca, T. Kucharzik, and D. T. Rubin, “Intestinal Ultrasound in the Assessment and Management of Inflammatory Bowel Disease: Is It Ready for Standard Practice?,” *Gastroenterology*, vol. 164, no. 6, pp. 851–855, May 2023, doi: 10.1053/j.gastro.2023.01.021.
- [16] C. Cueto *et al.*, “Stride: A flexible software platform for high-performance ultrasound computed tomography,” *Comput. Methods Programs Biomed.*, vol. 221, p. 106855, Jun. 2022, doi: 10.1016/j.cmpb.2022.106855.
- [17] K. Sastry *et al.*, “A method for the geometric calibration of ultrasound transducer arrays with arbitrary geometries,” *Photoacoustics*, vol. 32, p. 100520, Aug. 2023, doi: 10.1016/j.pacs.2023.100520.
- [18] S. B. Barnett, G. R. Ter Haar, M. C. Ziskin, H.-D. Rott, F. A. Duck, and K. Maeda, “International recommendations and guidelines for the safe use of diagnostic ultrasound in medicine,” *Ultrasound Med. Biol.*, vol. 26, no. 3, pp. 355–366, Mar. 2000, doi: 10.1016/S0301-5629(00)00204-0.